High-Performance Photodetector based on ReSe2/ PtSe2 van der Waals Heterojunction

Journal:	*ACS Applied Electronic Materials*
Manuscript ID	el-2023-00220n
Manuscript Type:	Article
Date Submitted by the Author:	20-Feb-2023
Complete List of Authors:	Song, Yi; USTC Li, Ming; Institute of Solid State Physics Chinese Academy of Sciences, Chen, Jiawang; Hefei Institutes of Physical Science Chinese Academy of Sciences Du, Yuchen; Anhui University Qin, Qinggang; Anhui University Du, Zengyan; University of Science and Technology of China, Zou, Fengxia; USTC Ma, XIaofei; University of Science and Technology of China Li, Liang; Chinese Academy of Sciences Hefei Institutes of Physical Science Institute of Solid State Physics, Li, Guanghai; Institute of Solid State Physics Chinese Academy of Sciences, Chinese Academy of Sciences

High-Performance Photodetector based on $ReSe_2$/ $PtSe_2$ van der Waals Heterojunction

Yi Song[1], Ming Li[1], Jiawang Chen[1], Yuchen Du[2], Qinggang Qin[2], Zengyan Du[1], Fengxia Zou[1], Xiaofei Ma[1], Liang li[1], Guanghai Li[1]**

[1]Key Laboratory of Materials Physics, Anhui Key Laboratory of Nanomaterials and Nanotechnology, Institute of Solid State Physics, Hefei Institutes of Physical Science, Chinese Academy of Sciences, Hefei 230031, P.R. China. University of Science and Technology of China, Hefei 230026, P. R. China

[2]Information Materials and Intelligent Sensing Laboratory of Anhui Province, Institutes of Physical Science and Information Technology, Anhui University, Hefei 230601, P. R. China

Keywords: heterostructure, ambipolar, $ReSe_2$, semimetal, photodetector

ABSTRACT: In recent years, heterojunction photodetectors constructed of two-dimensional materials with no overhanging bonds and lattice mismatches have attracted wide attention due to the advantages of integrating different materials. Here we report a high-performance photodetector with tunable dual auroral responses based on semiconductor ($ReSe_2$) and semimetal ($PtSe_2$) heterojunction, with a high reverse commutation ratio of 6.2×10^4 at room temperature. Under visible light irradiation, the photodetector with an open circuit voltage of 0.2 V and a short circuit current of 19 pA, and a high on/off ratio of 5.5×10^4, exhibits a clear photovoltaic effect. At the same time, the photodetector shows the photoelectric responsivity and detectivity of 153 mA/W and 7.72×10^{11} Jones, respectively. The photodetector also shows a large wideband optical detection capability between ultraviolet and near infrared light. Our work provides a model to develop future electronic and optoelectronic multifunctional devices based on 2D semiconductor and semimetal van der Waals heterojunction.

■INTRODUCTION

Photodetector plays an important role in many scenes in rapid developed science and technology. Because of widely applications in different fields such as medical imaging,[1] target recognition and tracking,[2] environmental monitoring,[3] chemistry,[4] machine vision systems,[5] and robot,[6] photodetector has aroused even more research interest. Traditional photodetectors are usually based on group IV or III-V semiconductors (such as silicon, germanium, etc.). Due to the limitations of these single materials, it is generally hard to meet the increasingly complex application needs in reality. Since the discovery of graphene, more and more high-performance photodetectors made of two-dimensional (2D) layered materials, with high responsivity and high detectivity have been reported.[7-19] For practical applications, a good photodetector should have high signal-to-noise ratio, short response time, high responsivity, and low or no practical application power dissipation.[20] Van der Waals heterostructures (vdWHs) made of 2D materials provide an innovative approach to solve above problems.[21] With no overhanging bonds and lattice mismatches, vdW heterojunctions can be formed by various 2D materials through vertical superposition, which provides an idea for the construction of vdWHs with unique properties through infinite combination of different two-dimensional materials.[22-27]

Transition metal dichalcogenides (TMDs) exist in the form of MX_2 in the 2D layered materials family. TMDs have the fascinating properties that the band structure varies with its thickness, and the band gap adjusts with its number of layers, and thus attract much attention.[28] $ReSe_2$ nanosheets with a twisted triclinic structure with ambipolar transport properties are a promising 2D material with outstanding optical and electrical properties.[29] As a typical representative of Group 6 TMDs, $ReSe_2$ is a layered and highly anisotropic semiconductor with a weak layer-dependent band gap between 1.24 eV and 1.09 eV.[30, 31] Nevertheless, the wide

depletion barrier of electron-hole recombination at the junction interface is hindered,[32, 33] and the performance of the photodetector based on 2D $ReSe_2$ is also limited due to the unbalanced concentrations between electrons and holes. How to solve this problem is undoubtedly a great challenge. Based on literatures, if we combine ambipolar $ReSe_2$ with semimetal 2D materials, such as $PtSe_2$, to form semiconductor-semimetal vdWH might solve this problem. As a representative member of the tenth group of TMDs, 2D semiconductor $PtSe_2$ has a band gap of 1.2 eV and 0.21 eV of monolayer and bilayer, respectively, but it shows semimetal behavior when the layer reaches three and above.[34-38] At room temperature, the carrier mobility of $PtSe_2$ can theoretically be as high as 4000 $cm^2\ V^{-1}\ s^{-1}$.[39] This makes $PtSe_2$ an extremely promising channel material for ultra-thin, flexible electronic devices. Selective controlling as either a semiconductor or a semimetal demonstrates the potential of 2D $ReSe_2$ in integration as a circuit component in two-dimensional circuits, used as both electrode and semiconductor channel, facilitating the formation of uniform semimetal-semiconductor contacts. But up to now, the Van der Waals heterojunction photodetectors combined $ReSe_2$ with semimetal materials are rarely involved and lack in-depth development in literatures.

In this work, a gate-voltage-regulated heterojunction photodiode combined 2D semiconductor $ReSe_2$ with 2D semimetal $PtSe_2$ is demonstrated. The semimetal $PtSe_2$ has high electron concentration and high electron mobility, which can be used as carrier selective contact,[40] and the semiconductor $ReSe_2$ is used as photoactive material. The photodiodes achieved a broadband optical response from ultraviolet (UV) to near-infrared (NIR) regions at room temperature. $ReSe_2/PtSe_2$ heterojunction diodes exhibit gate-adjustable bidirectional diode behavior. Under the control of gate voltage, the current rectification ratio is more than 6.2×10^4. The open-circuit voltage is as high as 0.2 V, and the short-circuit current is 19 pA, achieving the

high-light current to dark current ratio of 5.5×10^4. At the same time, under the laser irradiation at 635 nm, the heterojunction has an excellent responsivity and a high detectivity of 153 mA/W and 7.72×10^{11} Jones, respectively without bias voltage. The EQE is up to 30%, indicating the efficient separation of photogenerated electron-hole pairs.

■RESULTS AND DISCUSSION

Figs. 1a and b respectively show the schematic diagram of $ReSe_2/PtSe_2$ heterojunction structures superimposed on SiO_2/Si substrate and optical microscope image of the heterojunction device. The resulted $ReSe_2/PtSe_2$ vdWH device consists of mechanical stripping and polydimethylsiloxane assisted dry transfer (see the supporting information for the detailed manufacturing process of the device). The $ReSe_2/PtSe_2$ heterojunction is constructed by a few layers of $ReSe_2$ and $PtSe_2$ mechanically separated from the corresponding bulk material, as shown in Fig. 1a, performing form an exact transfer on the substrate via a micro nano transfer platform. As can be seen from the optical microscope images, Fig. 1b, a few layers of $ReSe_2$ film was superimposed on the $PtSe_2$ film with an overlapping area of about 17 μm^2, and then Au/Pt electrodes deposited on the $ReSe_2$ and $PtSe_2$ films. As $ReSe_2$ has a wider band gap than $PtSe_2$, the $ReSe_2$ film is stacked on top of $PtSe_2$ film for more efficient light absorption. The SiO_2/Si substrate with a thickness of 300 nm acts as the doped back gate of electrons or holes in $ReSe_2$ and $PtSe_2$ films. Notably, the performance of the device can be easily tested by depositing electrodes in the area near the junction. The results of measuring the heterojunction region by atomic force microscopy (AFM) are shown in Fig. 1d. The thickness information of the $ReSe_2$ and $PtSe_2$ films is displayed in the linear scanning contour of AFM image (Fig S1), and from which one can see that $ReSe_2$ film is about 6.3 nm thick, and thus its number of the layers is approximately 9,[41] while that of the $PtSe_2$ film is 5.9 nm and its number of layers is about 12.[42, 43] Raman scattering

measurements were performed on the device to ensure heterogeneous structure and material formation, and the results are shown in Fig. 1c. In the thin $ReSe_2$ region, the Raman signals caused by the in-plane vibration (E_g) is located at ≈118/123 cm^{-1} and the Raman signals at ≈158/172 cm^{-1} and ≈284/294 cm^{-1} are caused by the out-of-plane vibration (A_g) (Fig. 1c, blue line). These results are consistent with previous report for $ReSe_2$ film.[44] In the $PtSe_2$ region, the peak corresponding to the E_g phonon mode and the A_{1g} mode were respectively observed at 175 cm^{-1} and 205 cm^{-1} (Fig. 1c, red line), and the inconspicuous feature at ~230 cm^{-1} is attributed to an overlap between the E_u and A_{2u} modes, which are longitudinal optical (LO) modes of in-plane the and out-of-plane motions of platinum and selenium atoms, respectively. This is consistent with previous report for $PtSe_2$ film.[45] From Fig. 1c one can see all the Raman signals for both $ReSe_2$ and $PtSe_2$ appear on the heterojunction region (Fig. 1c, black line), and compared with the corresponding single material, there is no obvious peak shift, demonstrating that the two films forming the heterojunction region have high quality. These results also prove that the heterostructural region consists of the $ReSe_2$ and $PtSe_2$.

Subsequently, the electrical properties of individual $ReSe_2$ and $PtSe_2$ vdWH devices and $ReSe_2/PtSe_2$ vdW heterojunction devices are measured. Fig. 2a is a schematic diagram of a $ReSe_2/PtSe_2$ vdW heterojunction device used to measure electrical properties. As mentioned above, the $ReSe_2$ film with a larger band gap is placed on the top of $PtSe_2$ film for better photo absorption. In order to adjust the carrier density of each film, Si substrate acts as the back gate. The metal electrode deposited on the side of $ReSe_2$ and $PtSe_2$ are defined as the drain electrode and source electrode, respectively. In addition, two electrodes are attached to each $ReSe_2$ and $PtSe_2$ film, which makes it easier to study the properties of individual film of $ReSe_2$ and $PtSe_2$ and the $ReSe_2/PtSe_2$ heterojunction. The measured electrical characteristics of single $ReSe_2$ and $PtSe_2$

field-effect transistors (FETs) are shown in Figs. S2 and 3 in supporting information. The transfer curve of $ReSe_2$ FET exhibits that there is a large conduction current and ambipolar conduction under the control of gate voltage between -40 V and 40 V (Fig. S2c), where N-type conductance behavior is slightly stronger than P-type, which indicates that the Fermi level is close to the minimum conduction value of $ReSe_2$, and the electron density is higher than the hole density. The linear mode of I-V curve of the $PtSe_2$ FET (Fig. S3b) indicates that there is ohmic contact between $PtSe_2$ and the metal electrode, showing semimetal conductivity behavior of $PtSe_2$ film, which is consistent with previous report.[46] Fig. 2b shows the linear I_{ds}-V_{ds} curve of the $ReSe_2$/$PtSe_2$ vdWH device over the V_{ds} = ± 2V bias voltage range in a logarithmic scale. Extremely large reverse current and very low forward current can be observed, forming a clear reverse diode. The rectification ratio of the device can be obtained by calculating the ratio of reverse current to forward current. At room temperature, the rectifier ratio reached 4.7×10^2 without gate voltage. Fig. 2c shows the output characteristics of the $ReSe_2$/$PtSe_2$ vdWH device in the V_g = ± 30V gate voltage range. It can be found that the higher the gate voltage is, the better the rectifier performance of the device, regardless of whether the gate voltage is positive or negative The highest rectifying ratio of 6.2×10^4 is achieved at V_g = 30 V, an increase of two orders of magnitude compared to that without gate voltage. Comparing the output characteristics of the $ReSe_2$/$PtSe_2$ vdWH device with that of the isolated $ReSe_2$ vdWH device, one can see that the $ReSe_2$ film determines the conductivity of the $ReSe_2$/$PtSe_2$ vdWH device. The I_{ds}-V_g curve of the $ReSe_2$/$PtSe_2$ vdWH devices were measured to study the conductivity behavior of diodes, as shown in Fig. 2d. The ambipolar FET behavior of $ReSe_2$/$PtSe_2$ vdWH device shows that P-type and N-type doping can be obtained under the control of gate voltage, and the heterojunction diode can switch between pure P-type diode and pure N-type diode extremely well. The integrated transmission mechanism of

$ReSe_2/PtSe_2$ vdWH will be explained in detail by describing the band arrangement of $ReSe_2$ and $PtSe_2$ later.

The energy band information of $ReSe_2$ and $PtSe_2$ was obtained to study the transmission mechanism so that the behavior of the back-gate regulated rectifier of $ReSe_2/PtSe_2$ vdWH reverse diode will be further understood. First, the surface potential of $ReSe_2$ and $PtSe_2$ was measured by Kelvin Probe force microscopy (KPFM), upon which to determine their Fermi level difference and the result is shown in Fig. 3a. The KPFM measurement diagram is shown in Fig. S4. The KPFM measurement was performed using the RH-coated KPFM tip (Φ_{tip} = 4.98 eV) and the straddle-alignment was estimated. The average ΔV_{CPD} values of $ReSe_2$ and $PtSe_2$ films were obtained at 190 mV and 160 mV, respectively. The ΔV_{CPD} is defined as the difference between the KPFM tips and the work function of the sample. The functional values of $ReSe_2$ and $PtSe_2$ can be obtained by the following formula

$$\emptyset_s = \emptyset_{tip} - \Delta V_{CPD} \quad (1)$$

where Φ_{tip} and Φ_s are the KPFM tips and work function of the sample ($ReSe_2$ and $PtSe_2$), respectively. Thus, the work function of $ReSe_2$ and $PtSe_2$ films can be estimated, and the results are about 4.79 eV and 4.82 eV, respectively (Fig. 3b), and the difference of Fermi level between $ReSe_2$ and $PtSe_2$ is about 30 meV (0.03 eV). Figs. 3b and c show the band distribution before $ReSe_2$ and $PtSe_2$ contact and the band arrangement after contact to return to the equilibrium state. According to the KPFM measurement results, the electrons of $ReSe_2$ will drift into $PtSe_2$ and reach the equilibrium state when $ReSe_2$ and $PtSe_2$ are stacked vertically together. At this time, the electron density in $ReSe_2$ decreases, resulting in the formation of an obvious band bending electron depletion region on the side of $ReSe_2$, while the electrons in $PtSe_2$ will increase. This also means

that an internal electric field from $ReSe_2$ to $PtSe_2$ will be formed at the $ReSe_2/PtSe_2$ vdWH interface. Figure 3d-g shows the energy band arrangement of $ReSe_2/PtSe_2$ vdWH device under different conditions. For the obvious rectification behavior, $ReSe_2$ is modulated to heavy N type with the rise of Fermi level when the gate voltage is positive. Fig. 3d shows that, holes flow from $ReSe_2$ to $PtSe_2$ under positive bias voltage. As a result of the positive gate voltage, the holes in $ReSe_2$ are a few charge carriers, so a minor current is generated. Fig. 3e shows that when the bias voltage is negative, the internal electric field is weakened, the potential barrier in the heterojunction region is reduced, and electrons are transferred from the high-level $ReSe_2$ to the low-level $PtSe_2$, thus generating a larger current. According to these results, it is clear to find the minor forward current and large reverse current in the I-V characteristic curve of the back gate controlof $ReSe_2/PtSe_2$ vdWH device. This leads to heavily doped reverse diode with rectifier ratio of more than 10^4. As the positive V_g increases, the Fermi level of $ReSe_2$ gradually rises, which leads to more bending of the energy band, resulting in an increase in both forward and reverse current. The reverse current increases by a larger margin due to the positive gate voltage, so the rectification ratio increases with increasing gate voltage. $ReSe_2$ is modulated to heavy P type conductive behavior with the decrease of Fermi level due to the negative gate voltage. Fig. 3f shows that when the bias voltage is positive, the internal electric field is weakened, the potential barrier in the junction area is lowered, and holes flow from $ReSe_2$ to $PtSe_2$, thus generating a large current. As shown in Fig. 3g, under negative bias, electrons are transferred from high energy $ReSe_2$ to low energy $PtSe_2$. As a result of the negative gate voltage, the electrons in $ReSe_2$ are minority carriers, so a small current is generated. With the increase of negative V_g, the Fermi level of $ReSe_2$ is reduced, which leads to more bending of the energy band. However, the density of minority carriers in $ReSe_2$ gradually decreases, so the reverse current decreases and the forward current

increases. According to the above results, it is clear to find the small reverse current and large forward current in the back gate related I-V curve of $ReSe_2/PtSe_2$ vdWH device.

Next, in order to the explore its potential applications, the photoelectric characteristics of the $ReSe_2/PtSe_2$ vdWH diode are systematically studied. Fig. 4a shows the photodetector irradiated by a 635 nm laser through schematic diagram. It is worth noting that all the photoelectric characteristics are measured without applying the gate voltage (V_g = 0 V), unless specially emphasized. The photoresponse range of the $ReSe_2/PtSe_2$ vdWH device was tested by irradiating the heterostructure with the same incident laser power of 3.6 mW with lasers with the wavelength of 405, 635, 780 and 940 nm. The I-V curves of the heterojunction in the dark are shown in Fig. 4d, and an obvious wavelength dependence of the photoresponse can be observed. For the tested four wavelengths of laser, the best photoreponse of the $ReSe_2/PtSe_2$ vdWH device is under the irradiation of λ = 635 nm laser. Thus, the 635 nm laser was selected for the subsequent tests. The photoreponse curves of the $ReSe_2/PtSe_2$ vdWH photodiode under 635 nm laser irradiation with different laser power densities and dark state when V_g = 0 V was shown in Fig. 4b. The photoresponse characteristics of the device to laser irradiation of the other three wavelengths are shown in Fig. S5. Under laser irradiation, no matter in the positive bias region or negative bias region, a significant increase in photocurrent can be observed, and positive bias region shows a higher sensitivity to laser power. The light on/off ratio of the device is about 10^3 at zero bias voltage when the laser power density is 7.29 mW/cm^2. The laser irradiation passes from top $ReSe_2$ film to bottom $PtSe_2$ film. According to the photoelectric performance of the $PtSe_2$ film (Fig. S3, supporting information), the difference between light and dark currents is negligible. It can be inferred that only the channels in the top $ReSe_2$ film produce electron-hole pairs. The I-V characteristics of the $ReSe_2/PtSe_2$ vdWH device in the small range bias voltage under laser

irradiation with different laser power densities are shown in Fig. 4c. It is clear to found that short-circuit current is positive and open-circuit voltage is negative, and under the influence of the increased laser power density, the short-circuit current increases. For high-performance photodetectors, the response speed is an extremely important parameter. The I-T curves of the photodetector under 635 nm laser irradiation with different laser power densities without bias voltage is shown in Fig. S6a, from which one can see under the laser irradiation of periodic switch, the photocurrent can be stabilized in a short time. The one-period I-T curve extracted from Fig. S6a is shown in Fig. S6b. The response speed can be measured by the rise time (defined as the time required for the photocurrent to rise from 10% to 90%) or the decay time (the time required for the photocurrent to fall from 90% to 10%). From Fig. S6b, one can see obtained that the rise time of the $ReSe_2/PtSe_2$ vdWH device is about 0.8 s and the decay time is about 0.7 s. A great improvement in response speed is achieved for the $ReSe_2/PtSe_2$ vdWH device as compared with that for the single $ReSe_2$ device[41]. The photoresponse at V_g = -40 V was measured so that the influence of the gate voltage on the photoelectric performance of the $ReSe_2/PtSe_2$ vdWH devices can be further explored. As Fig. 4e shown, the logarithmic form of output characteristic curves of the $ReSe_2/PtSe_2$ vdWH device under 635 nm laser irradiation with different laser power densities and at dark state when -40 V gate voltage is applied. Different from V_g = 0 V, when -40 V gated voltage is applied, the increase of photocurrent is mainly shown in the region where $V_{ds} < 0$ V, and a high on/off ratio of more than 5.5×10^4 at negative bias is achieved. The I-V characteristics of the $ReSe_2/PtSe_2$ vdWH device in the small range bias voltage under laser irradiation with different laser power densities when -40 V gate voltage is applied are shown in Fig. 4f. Under the influence of -40 V gate voltage, the conductive behavior of $ReSe_2$ changes to heavy P-type with the decrease of Fermi level. At this time, due to the internal electric field, the electrons drift to the

$PtSe_2$ side and enter the source electrode, while the holes drift to the $ReSe_2$ side and enter the drain electrode. Therefore, negative I_{sc} and positive V_{oc} can be found in Fig. 4f. When the laser power density is 7.29 mW/cm^2, the short circuit current of 19 pA and open circuit voltage of 0.2 V are obtained.

The net photocurrent I_{ph} under different laser power densities was tested when V_g = 0V and V_g = -40 V to explore the mechanism of photocurrent generation, and the results are shown in Figs. 5a and d, respectively.

$$I_{ph} = I_{ds} - I_{dark} \quad (2)$$

where I_{ds} and I_{dark} is the current of the device under light and dark state, respectively. In Figs 5a and d, the black point is the data measured in the experiment, and the red line is the curve obtained by fitting the power-law formula

$$I_{ph} = \alpha P^{\theta} \quad (3)$$

In the formula α is a constant, P is the laser power density of the incident laser, and θ is the power-law index. The value of θ calculated according to the fitting results is about 0.47 and 0.85 with V_g = 0 V and -40 V, respectively. The photocurrent is dictated by the photogating effect referring to trap states, and by the photoconductive effect, respectively, when $\theta = 0$ and $\theta = 1$.[47] Above results indicate that these the photocurrent of the $ReSe_2/PtSe_2$ vdWH device is determined by these two effects. The photoelectric mechanism of the $ReSe_2/PtSe_2$ vdWH device can be understood through the energy band diagram shown in Figs. 5c and f. Without gate voltage, the top $ReSe_2$ film mainly produces photogenerated electron hole pairs. Fig. 4c shows that due to large built-in electric field in the single-side consumption area of $ReSe_2$, the electrons drift to the $ReSe_2$ side and are gathered by the drain electrode, while the holes drift to the $PtSe_2$ side and are gathered by the source

electrode, thus generating positive I_{sc} and negative V_{oc}. Generally when a positive bias voltage is applied, electrons flow from $PtSe_2$ to $ReSe_2$. However, according to the photoelectric performance of the $PtSe_2$, it can be known that the $PtSe_2$ film is not sensitive to laser irradiation, and the photogenerated electron hole pairs are almost negligible. Therefore, in the positive bias area of Fig. 4e, it can be observed that the photoelectric current generated by the $ReSe_2/PtSe_2$ vdWH device under laser irradiation is not much higher than the dark current generated in the dark state. When a negative bias voltage is applied, $ReSe_2$ is excited to generate electron hole pairs, and the electrons flow to $PtSe_2$, thus generating a larger photocurrent compared to the dark state, as shown in Fig.5f. Responsivity (R) and detectivity (D^*) play an important role in the quantitative evaluation of high-performance photodetectors, and can be expressed as

$$R = \frac{I_{ph}}{P_{in}} \cdot A \quad (4)$$

$$D^* = \frac{R \cdot \sqrt{A}}{\sqrt{2e \cdot I_{dark}}} \quad (5)$$

where I_{ph} is the net photo current described above, A is the effective illumination area of the photodetector, P_{in} is the power density of the irradiated laser, and e is the unit charge. Figs. 5b and e show the functions of R and D^* to laser power densities when the gate voltage is 0 V and -40 V, respectively, without bias voltage under 635 nm laser irradiation. The increase of laser power density leads to the decrease of R and D^*, indicating that trap states capture the photogenerated electrons and reduce the possibility of photogenerated electrons recombination. From these two figures one can obtained that the maximum R is about 153 mA/W and the maximum D^* is about 7.72×10^{11} Jones, which are better than the value in some previous reported literatures (Table S1), demonstrating excellent performance of the $ReSe_2/PtSe_2$ vdWH device. External quantum

efficiency (EQE) and power conversion efficiency (PCE) are also very important parameters. PCE can be obtained by the formula

$$\mathrm{PCE} = \frac{P_{max}}{P_{in}} \quad (6)$$

where P_{max} is the maximum electrical power generated by the photodetector under laser irradiation and P_{in} is the effective power of the laser irradiation.[48] The EQE can be interpreted as the ratio of the number of photons emitted in the plane per unit time to the electron-hole pairs injected in the plane per unit time, which can be obtained by formula

$$\mathrm{EQE} = \frac{Rhc}{e\lambda} \quad (7)$$

where h is the Planck constant, the value of c is the speed of light and λ is the wavelength of the laser.[26] From the calculated results of the PCE and EQE of the $ReSe_2/PtSe_2$ vdWH device when the gate voltage is 0 V and -40 V under 635 nm laser irradiation without bias voltage shown in Fig. S7, one can see the maximum values of PCE and EQE were $1.5x10^{-3}$% and 30%, respectively, indicating efficient separation of photogenerated electron-hole pairs in the $ReSe_2/PtSe_2$ vdWH device.

■CONCLUSIONS

In summary, for the first time a high-performance photodetector based on 2D semiconductor $ReSe_2$ and 2D semimetal $PtSe_2$ van der Waals heterojunction was proposed and successfully constructed. The $ReSe_2$ serves as photoactive material, while $PtSe_2$ serves as carriers selective contact. The polarity of the photodetector can be adjusted by the gate voltage V_g. A high reverse rectifier ratio of 6.2×10^4 can be realized at room temperature. The short-circuit current and open-circuit voltage are 19 pA and 0.2 V, respectively, and the light on/off ratio is over 5.5×10^4 under proper condition. The photodetector has a responsivity of 153 mA/W and a detectivity of 7.72×10^{11} Jones. The photodetector also shows a wideband optical detection from ultraviolet to near infrared light. Our results demonstrated that 2D semiconductors and 2D semimetals have great potential in the development of high-performance photodetectors.

■EXPERIMENTAL SECTION

Device Fabrication. The method of constructing $ReSe_2/PtSe_2$ vdWH device was the dry transfer method with PDMS as the carrier and the mechanical stripping method. First, the corresponding films were prepared from the bulk of $ReSe_2$ and $PtSe_2$ by mechanical stripping with adhesive tape, and then the $ReSe_2$ and $PtSe_2$ films were transferred to the Si substrate covered with 300 nm SiO_2 using PDMS as the carrier. After that, the electrode pattern is drawn by electron beam lithography (EBL, eLINE Plus, Raith), and then Ti (thickness of 15 nm) and Au (thickness of 60 nm) are deposited on the substrate by electron beam evaporation and thermal evaporation. Finally, the electroplating device is processed in acetone under the standard stripping process.

Device Characterization and Testing. The optical microscope (WMJ-9688) was used to study $ReSe_2/PtSe_2$ vdWH device. The Raman spectrum were measured using a laser source with a wavelength of 532 nm and a Raman/photoluminescence (PL) system (FST2-Ahdx-DZ) equipped with a monochromator. The film thickness and surface potential of the $ReSe_2$ and $PtSe_2$ films were measured by KPFM (Hitachi AFM5500M). The electrical performance of $ReSe_2$ and $PtSe_2$ vdWH devices was measured by using a semiconductor device parameter analyzer (Keithley 4200A-SCS) in the detection station (HFS600E-PB4). In the process of optical response measurement, 635 nm laser was always irradiated on the effective area of the device. The above measurement results were obtained at room temperature.

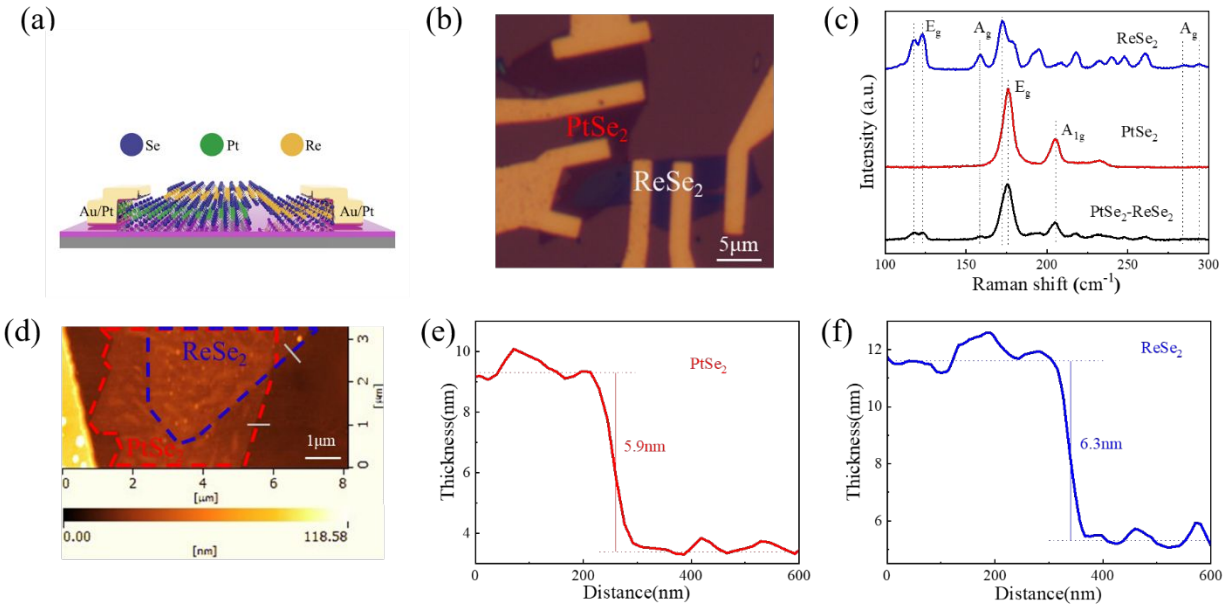

Figure 1. Optical characterizations and AFM measurements of the $ReSe_2/PtSe_2$ vdWH heterojunction. (a) Schematic diagram of $ReSe_2/PtSe_2$ heterostructures superimposed on SiO_2/Si substrates, (b) optical microscope image of the heterojunction. (c) Raman spectra of $ReSe_2$ and $PtSe_2$ films, and $ReSe_2/PtSe_2$ vdWH heterojunction. (d) AFM measurement results of $ReSe_2/PtSe_2$ vdWH. Thickness information of $ReSe_2$ film (e) and $PtSe_2$ film (f).

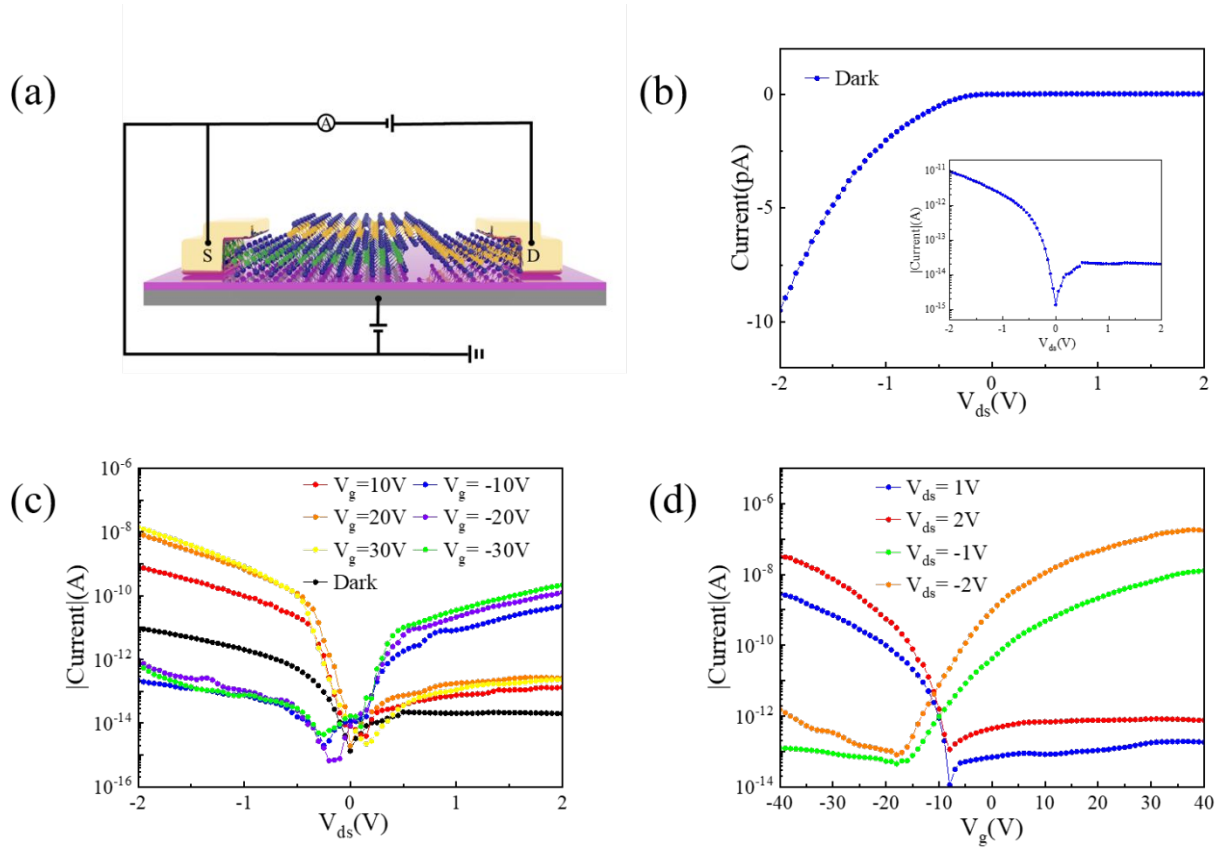

Figure 2. Electrical properties of the $ReSe_2/PtSe_2$ vdWH device. (a) Schematic diagram of a $ReSe_2/PtSe_2$ vdWH device used to measure electrical properties. (b) Linear I_{ds}-V_{ds} characteristics of $ReSe_2/PtSe_2$ vdWH device in the range V_{ds} = ±2 V. The I_{ds}-V_{ds} characteristics is on logarithmic scale. (c) Output characteristics of $ReSe_2/PtSe_2$ vdWH devices on logarithmic scales in the V_g = ±30 V range. (d) I_{ds}-V_g characteristics of $ReSe_2/PtSe_2$ vdWH device at different bias voltages.

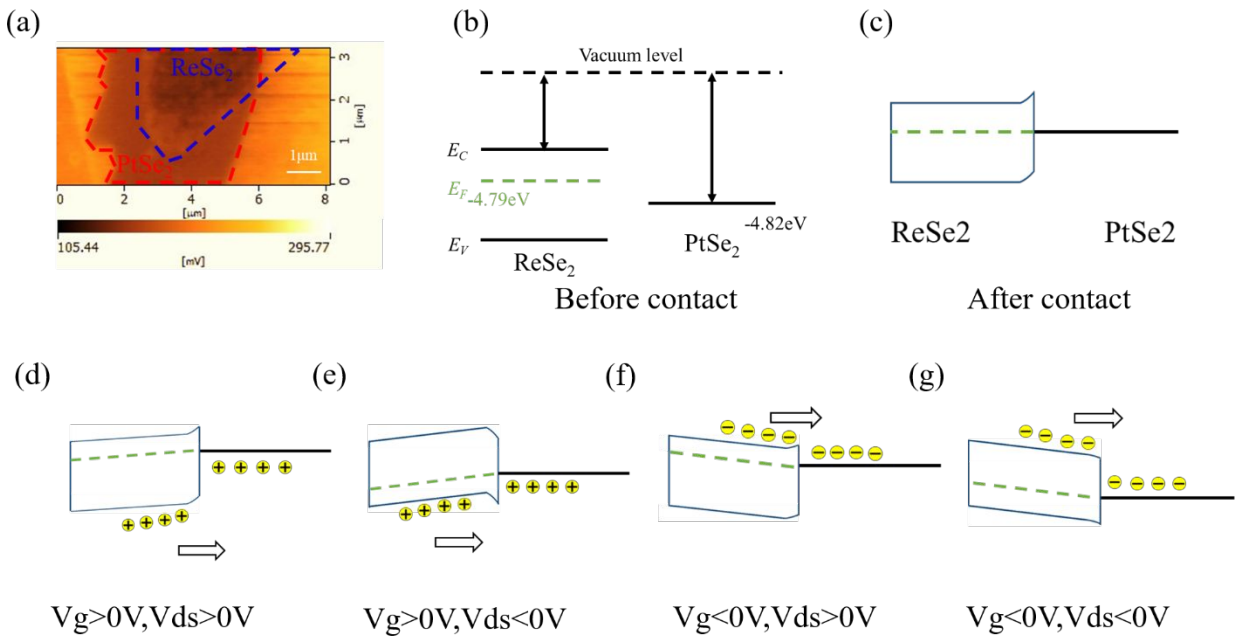

Figure 3. KPFM characterization and schematic energy band diagrams of the $ReSe_2/PtSe_2$ vdWH device. (a) KPFM image of the $ReSe_2/PtSe_2$ vdWH. (b) (c) Band structure of $ReSe_2/PtSe_2$ vdWH before and after contact. (d)-(g) Energy band diagrams of the $ReSe_2/PtSe_2$ vdWH device under different bias voltages V_{ds} and gate voltages V_g.

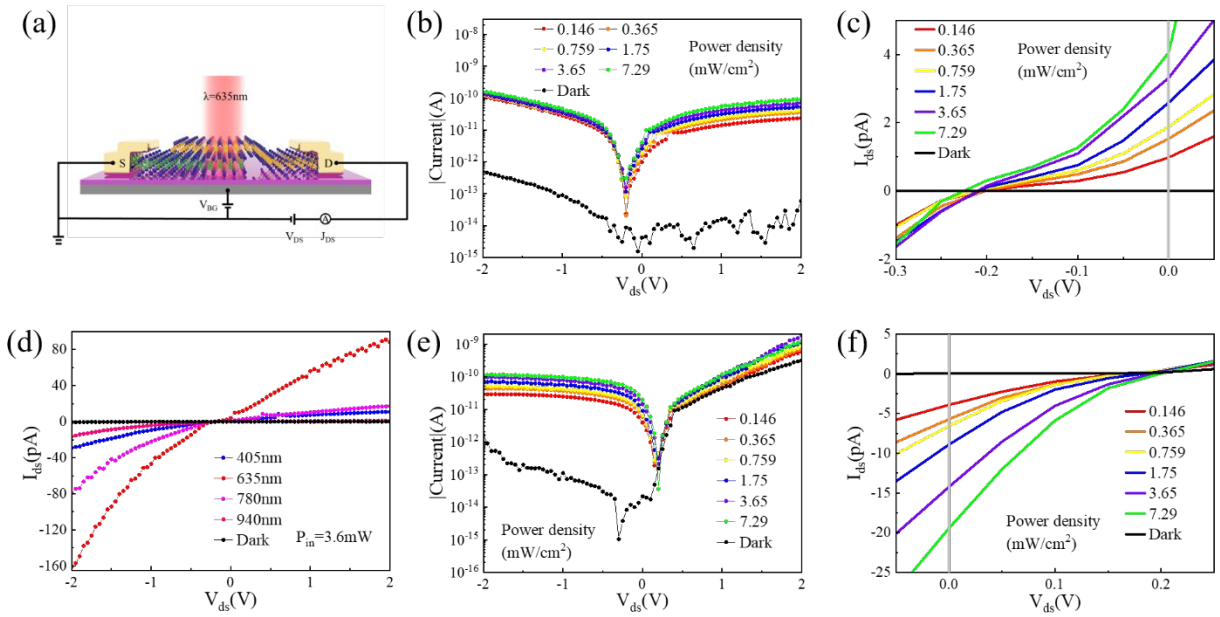

Figure 4. Photoresponse characteristics of the $ReSe_2/PtSe_2$ vdWH device. (a) Schematic diagram of a heterojunction irradiated by a 635 nm laser. (b) (c) When $V_g = 0$ V, I_{ds}-V_{ds} curve of the device under 635 nm laser irradiation with different power densities and I_{ds}-V_{ds} curve under small bias voltage. (d) I_{ds}-V_{ds} characteristics of the $ReSe_2/PtSe_2$ vdWH device measured in darkness and under illumination at different wavelengths with 3.6 mW incident laser power. (e) and (f) When $V_g = -40$ V, I_{ds}-V_{ds} curve of the device under 635 nm laser irradiation with different power densities and the I_{ds}-V_{ds} curve under small bias voltage.

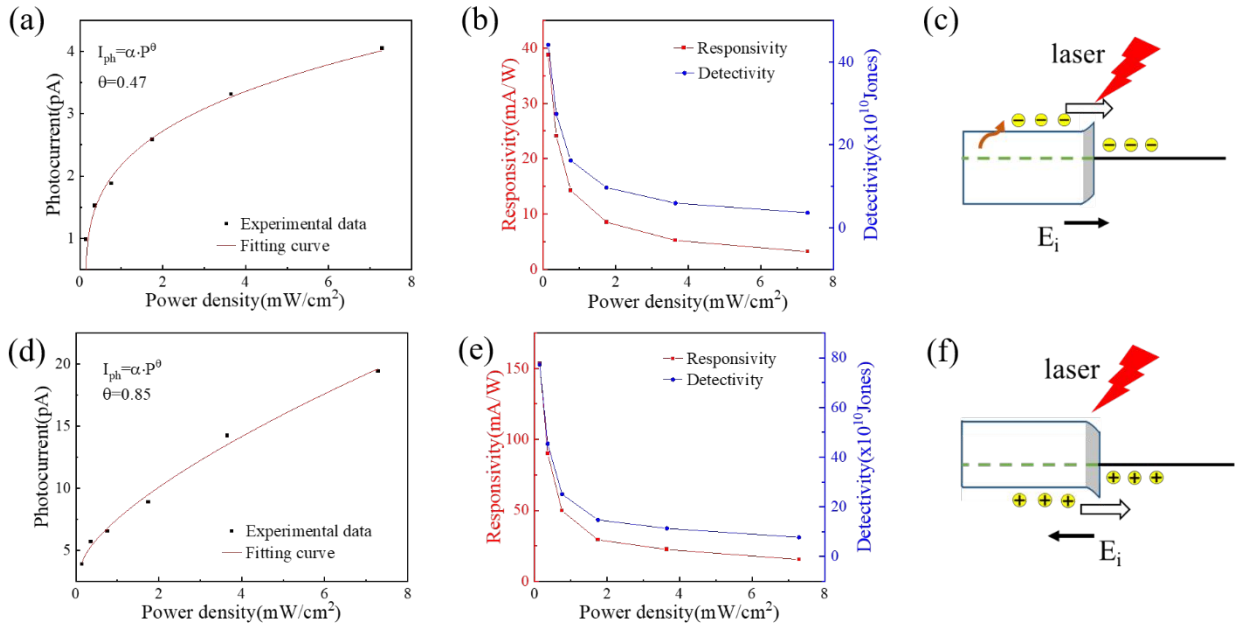

Figure 5. Input light power density dependence of the photocurrent I_{ph} of the $ReSe_2/PtSe_2$ vdWH device under incident laser (λ = 635 nm) (black dots) , the red lines show the best-fitted results at (a) V_g = 0 V and (d) V_g = -40 V. Laser power density (λ = 635 nm) dependent responsivity and detectivity at (b) V_g = 0 V and (e) V_g = -40 V. Photogenerated carrier band diagram of the heterojunction without bias voltage at (c) V_g = 0 V and (d) V_g = -40 V

ASSOCIATED CONTENT

Supporting Information

The detailed experimental process is shown in the supporting information.

Experimental section

Figure S1. AFM test results of $ReSe_2$ and $PtSe_2$.

Figure S2. Electrical properties of a single $ReSe_2$ FET.

Figure S3. Electrical properties of a single $PtSe_2$ FET.

Figure S4. Schematic of the KPFM measurement.

Figure S5. Photoresponse characteristics of $ReSe_2/PtSe_2$ vdWH devices.

Table S1. Comprehensive comparison of the critical parameters of fabricated $ReSe_2/PtSe_2$ vdWHs with previously reported $ReSe_2$ based photodetectors.

AUTHOR INFORMATION

Corresponding Author

* Corresponding author (email: liliang@issp.ac.cn)

* Corresponding author (email: ghli@issp.ac.cn)

Author Contributions

L.L. and G.H.L. supervised the project. Y.S and L.L. proposed the project. Y.S, L.L., and J.W.C. designed the experiments. F.X.Z. prepared bulk materials. Z.Y.D exfoliated 2D materials and

stacked heterostructures. Under supervision of Y.C.D, Q.G.Q. made electrode patterns using EBL. Q.G.Q. made electrodes by metal evaporation coating. Under supervision of Y.S., X.F.M. performed Raman spectra measurement. Under supervision of M.L. performed AFM/KPFM measurement. Y.S. performed the electrical characterization supervised by J.W.C.. L.L., J.W.C., Y.S., M.L., Z.Y.D. and Y.C.D. analyzed the results. Y.S and Z.Y.D. drew schematic diagrams. All authors discussed the results and provided constructive comments on the manuscript.

Funding Sources

This work is supported by the Collaborative Innovation Program of Hefei Science Center of Chinese Academy of Sciences (2022HSC-CIP019), the Pioneer Hundred Talents Program of Chinese Academy of Sciences (E24BHD17), the open fund of Information Materials and Intelligent Sensing Laboratory of Anhui Province (Grant No. IMIS202201), and the State Key Laboratory of Materials Processing and Die & Mould Technology, Huazhong University of Science and Technology (P2023-011).

Notes

The authors declare no competing financial interest.

REFERENCES

(1) Wu, Y. L.; Fukuda, K.; Yokota, T.; Someya, T. A Highly Responsive Organic Image Sensor Based on a Two-Terminal Organic Photodetector with Photomultiplication. *Adv. Mater.* **2019**, *31* (43), 7.

(2) Rogalski, A.; Antoszewski, J.; Faraone, L. Third-generation infrared photodetector arrays. *J. Appl. Phys.* **2009**, *105* (9), 44.

(3) Konstantatos, G.; Sargent, E. H. Nanostructured materials for photon detection. *Nat. Nanotechnol.* **2010**, *5* (6), 391-400.

(4) Abid; Sehrawat, P.; Islam, S. S.; Gulati, P.; Talib, M.; Mishra, P.; Khanuja, M. Development of highly sensitive optical sensor from carbon nanotube-alumina nanocomposite free-standing films: CNTs loading dependence sensor performance Analysis. *Sensors and Actuators a-Physical* **2018**, *269*, 62-69.

(5) Wu, P. S.; He, T.; Zhu, H.; Wang, Y.; Li, Q.; Wang, Z.; Fu, X.; Wang, F.; Wang, P.; Shan, C. X.; et al. Next-generation machine vision systems incorporating two-dimensional materials: Progress and perspectives. *Infomat* **2022**, *4* (1).

(6) Xie, M. Y.; Hisano, K.; Zhu, M. Z.; Toyoshi, T.; Pan, M.; Okada, S.; Tsutsumi, O.; Kawamura, S.; Bowen, C. Flexible Multifunctional Sensors for Wearable and Robotic Applications. *Adv. Mater. Technol.* **2019**, *4* (3), 29.

(7) Qi, P. F.; Luo, Y.; Li, W.; Cheng, Y.; Shan, H. Y.; Wang, X. L.; Liu, Z.; Ajayan, P. M.; Lou, J.; Hou, Y. L.; et al. Remote Lightening and Ultrafast Transition: Intrinsic Modulation of Exciton Spatiotemporal Dynamics in Monolayer MoS2. *ACS Nano* **2020**, *14* (6), 6897-6905.

(8) Resta, G. V.; Balaji, Y.; Lin, D.; Radu, I. P.; Catthoor, F.; Gaillardon, P. E.; De Micheli, G. Doping-Free Complementary Logic Gates Enabled by Two-Dimensional Polarity - Controllable Transistors. *ACS Nano* **2018**, *12* (7), 7039-7047.

(9) Zhang, X. K.; Liao, Q. L.; Kang, Z.; Liu, B. S.; Ou, Y.; Du, J. L.; Xiao, J. K.; Gao, L.; Shan, H. Y.; Luo, Y.; et al. Self-Healing Originated van der Waals Homojunctions with Strong Interlayer Coupling for High-Performance Photodiodes. *ACS Nano* **2019**, *13* (3), 3280-3291.

(10) Feng, X.; Sun, Z. D.; Pei, K.; Han, W.; Wang, F. K.; Luo, P.; Su, J. W.; Zuo, N.; Liu, G. H.; Li, H. Q.; et al. 2D Inorganic Bimolecular Crystals with Strong In-Plane Anisotropy for Second-Order Nonlinear Optics. *Adv. Mater.* **2020**, *32* (32), 9.

(11) Li, L.; Wang, W. K.; Gong, P. L.; Zhu, X. D.; Deng, B.; Shi, X. Q.; Gao, G. Y.; Li, H. Q.; Zhai, T. Y. 2D GeP: An Unexploited Low-Symmetry Semiconductor with Strong In-Plane Anisotropy. *Adv. Mater.* **2018**, *30* (14), 9.

(12) Ma, Z. Z.; Shi, Z. F.; Yang, D. W.; Li, Y. W.; Zhang, F.; Wang, L. T.; Chen, X.; Wu, D.; Tian, Y. T.; Zhang, Y.; et al. High Color-Rendering Index and Stable White Light-Emitting Diodes by Assembling Two Broadband Emissive Self-Trapped Excitons. *Adv. Mater.* **2021**, *33* (2), 10.

(13) Du, J. L.; Liao, Q. L.; Liu, B. S.; Zhang, X. K.; Yu, H. H.; Ou, Y.; Xiao, J. K.; Kang, Z.; Si, H. N.; Zhang, Z.; et al. Gate-Controlled Polarity-Reversible Photodiodes with Ambipolar 2D Semiconductors. *Adv. Funct. Mater.* **2021**, *31* (8), 10.

(14) Zhang, F.; Ma, Z. Z.; Shi, Z. F.; Chen, X.; Wu, D.; Li, X. J.; Shan, C. X. Recent Advances and Opportunities of Lead-Free Perovskite Nanocrystal for Optoelectronic Application. *Energy Mater. Adv.* **2021**, *2021*, 38.

(15) Cao, W.; Jiang, J. K.; Xie, X. J.; Pal, A.; Chu, J. H.; Kang, J. H.; Banerjee, K. 2-D Layered Materials for Next-Generation Electronics: Opportunities and Challenges. *IEEE Trans. Electron Devices* **2018**, *65* (10), 4109-4121.

(16) Li, L.; Han, W.; Pi, L. J.; Niu, P.; Han, J. B.; Wang, C. L.; Su, B.; Li, H. Q.; Xiong, J.; Bando, Y.; et al. Emerging in-plane anisotropic two-dimensional materials. *Infomat* **2019**, *1* (1), 54-73.

(17) Lee, J.; Duong, N. T.; Bang, S.; Park, C.; Nguyen, D. A.; Jeon, H.; Jang, J.; Oh, H. M.; Jeong, M. S. Modulation of Junction Modes in SnSe2/MoTe2 Broken-Gap van der Waals Heterostructure for Multifunctional Devices. *Nano Lett.* **2020**, *20* (4), 2370-2377.

(18) Chhowalla, M.; Shin, H. S.; Eda, G.; Li, L. J.; Loh, K. P.; Zhang, H. The chemistry of two-dimensional layered transition metal dichalcogenide nanosheets. *Nat. Chem.* **2013**, *5* (4), 263-275.

(19) Han, W.; Huang, P.; Li, L.; Wang, F. K.; Luo, P.; Liu, K. L.; Zhou, X.; Li, H. Q.; Zhang, X. W.; Cui, Y.; et al. Two-dimensional inorganic molecular crystals. *Nat. Commun.* **2019**, *10*, 10.

(20) Konstantatos, G. Current status and technological prospect of photodetectors based on two-dimensional materials. *Nat. Commun.* **2018**, *9*, 3.

(21) Liu, Y.; Huang, Y.; Duan, X. F. Van der Waals integration before and beyond two-dimensional materials. *Nature* **2019**, *567* (7748), 323-333.

(22) Wu, F.; Xia, H.; Sun, H. D.; Zhang, J. W.; Gong, F.; Wang, Z.; Chen, L.; Wang, P.; Long, M. S.; Wu, X.; et al. AsP/InSe Van der Waals Tunneling Heterojunctions with Ultrahigh Reverse Rectification Ratio and High Photosensitivity. *Adv. Funct. Mater.* **2019**, *29* (12), 9.

(23) Afzal, A. M.; Iqbal, M. Z.; Dastgeer, G.; Nazir, G.; Eom, J. Ultrafast and Highly Stable Photodetectors Based on p-GeSe/n-ReSe2 Heterostructures. *ACS Appl. Mater. Interfaces* **2021**, *13* (40), 47882-47894.

(24) Tan, C. Y.; Yin, S. Q.; Chen, J. W.; Lu, Y.; Wei, W. S.; Du, H. F.; Liu, K. L.; Wang, F. K.; Zhai, T. Y.; Li, L. Broken-Gap PtS2/WSe2 van der Waals Heterojunction with Ultrahigh Reverse Rectification and Fast Photoresponse. *ACS Nano* **2021**, *15* (5), 8328-8337.

(25) Ahmad, W.; Liu, J. D.; Jiang, J. Z.; Hao, Q. Y.; Wu, D.; Ke, Y. X.; Gan, H. B.; Laxmi, V.; Ouyang, Z. B.; Ouyang, F. P.; et al. Strong Interlayer Transition in Few-Layer InSe/PdSe2 van der Waals Heterostructure for Near-Infrared Photodetection. *Adv. Funct. Mater.* **2021**, *31* (43), 8.

(26) Lei, T.; Tu, H. Y.; Lv, W. M.; Ma, H. X.; Wang, J. C.; Hu, R.; Wang, Q. T.; Zhang, L. K.; Fang, B.; Liu, Z. Y.; et al. Ambipolar Photoresponsivity in an Ultrasensitive Photodetector Based on a WSe2/InSe Heterostructure by a Photogating Effect. *ACS Appl. Mater. Interfaces* **2021**, *13* (42), 50213-50219.

(27) Chen, Y.; Wang, X. D.; Wu, G. J.; Wang, Z.; Fang, H. H.; Lin, T.; Sun, S.; Shen, H.; Hu, W. D.; Wang, J. L.; et al. High-Performance Photovoltaic Detector Based on MoTe2/MoS2 Van der Waals Heterostructure. *Small* **2018**, *14* (9), 7.

(28) Koppens, F. H. L.; Mueller, T.; Avouris, P.; Ferrari, A. C.; Vitiello, M. S.; Polini, M. Photodetectors based on graphene, other two-dimensional materials and hybrid systems. *Nat. Nanotechnol.* **2014**, *9* (10), 780-793.

(29) Jariwala, B.; Voiry, D.; Jindal, A.; Chalke, B. A.; Bapat, R.; Thamizhavel, A.; Chhowalla, M.; Deshmukh, M.; Bhattacharya, A. Synthesis and Characterization of ReS2 and ReSe2 Layered Chalcogenide Single Crystals. *Chem. Mater.* **2016**, *28* (10), 3352-3359.

(30) Yang, S. X.; Tongay, S.; Li, Y.; Yue, Q.; Xia, J. B.; Li, S. S.; Li, J. B.; Wei, S. H. Layer-dependent electrical and optoelectronic responses of ReSe2 nanosheet transistors. *Nanoscale* **2014**, *6* (13), 7226-7231.

(31) Cui, F. F.; Li, X. B.; Feng, Q. L.; Yin, J. B.; Zhou, L.; Liu, D. Y.; Liu, K. Q.; He, X. X.; Liang, X.; Liu, S. Z.; et al. Epitaxial growth of large-area and highly crystalline anisotropic ReSe2 atomic layer. *Nano Res.* **2017**, *10* (8), 2732-2742.

(32) Lee, C. H.; Lee, G. H.; van der Zande, A. M.; Chen, W. C.; Li, Y. L.; Han, M. Y.; Cui, X.; Arefe, G.; Nuckolls, C.; Heinz, T. F.; et al. Atomically thin p-n junctions with van der Waals heterointerfaces. *Nat. Nanotechnol.* **2014**, *9* (9), 676-681.

(33) Furchi, M. M.; Pospischil, A.; Libisch, F.; Burgdorfer, J.; Mueller, T. Photovoltaic Effect in an Electrically Tunable van der Waals Heterojunction. *Nano Lett.* **2014**, *14* (8), 4785-4791.

(34) Wang, Y. L.; Li, L. F.; Yao, W.; Song, S. R.; Sun, J. T.; Pan, J. B.; Ren, X.; Li, C.; Okunishi, E.; Wang, Y. Q.; et al. Monolayer PtSe2, a New Semiconducting Transition-Metal-Dichalcogenide, Epitaxially Grown by Direct Selenization of Pt. *Nano Lett.* **2015**, *15* (6), 4013-4018.

(35) Wang, G. Z.; Wang, Z. Z.; McEvoy, N.; Fan, P.; Blau, W. J. Layered PtSe2 for Sensing, Photonic, and (Opto-)Electronic Applications. *Adv. Mater.* **2021**, *33* (1), 23.

(36) Zibouche, N.; Kuc, A.; Miró, P.; Heine, T. Noble-Metal Chalcogenide Nanotubes. *Inorganics* **2014**, *2* (4), 556-564.

(37) Villaos, R. A. B.; Crisostomo, C. P.; Huang, Z. Q.; Huang, S. M.; Padama, A. A. B.; Albao, M. A.; Lin, H.; Chuang, F. C. Thickness dependent electronic properties of Pt dichalcogenides. *npj 2D Mater. Appl.* **2019**, *3*, 8.

(38) Chen, E.; Xu, W.; Chen, J.; Warner, J. H. 2D layered noble metal dichalcogenides (Pt, Pd, Se, S) for electronics and energy applications. *Mater. Today Adv.* **2020**, *7*, 35.

(39) Xu, H.; Zhang, H. M.; Liu, Y. W.; Zhang, S. M.; Sun, Y. Y.; Guo, Z. X.; Sheng, Y. C.; Wang, X. D.; Luo, C.; Wu, X.; et al. Controlled Doping of Wafer-Scale PtSe2 Films for Device Application. *Adv. Funct. Mater.* **2019**, *29* (4), 8.

(40) Hu, Z. H.; Liu, X.; Hernandez-Martinez, P. L.; Zhang, S. S.; Gu, P.; Du, W.; Xu, W. G.; Demir, H. V.; Liu, H. Y.; Xiong, Q. H. Interfacial charge and energy transfer in van der Waals heterojunctions. *Infomat* **2022**, *4* (3).

(41) Hafeez, M.; Gan, L.; Li, H. Q.; Ma, Y.; Zhai, T. Y. Chemical Vapor Deposition Synthesis of Ultrathin Hexagonal ReSe2 Flakes for Anisotropic Raman Property and Optoelectronic Application. *Adv. Mater.* **2016**, *28* (37), 8296-8301.

(42) Zheng, H. S.; Choi, Y.; Baniasadi, F.; Hu, D. K.; Jiao, L. Y.; Park, K.; Tao, C. G. Visualization of point defects in ultrathin layered 1T-PtSe2. *2D Mater.* **2019**, *6* (4), 9.

(43) Yim, C.; Passi, V.; Lemme, M. C.; Duesberg, G. S.; Coileain, C. O.; Pallecchi, E.; Fadil, D.; McEvoy, N. Electrical devices from top-down structured platinum diselenide films. *npj 2D Mater. Appl.* **2018**, *2*, 7.

(44) Mathew, R. J.; Cheng, K. H.; Hsu, C. H.; Chand, P. K.; Inbaraj, C. R. P.; Peng, Y. L.; Yang, J. Y.; Lee, C. H.; Chen, Y. T. Near-Infrared Electroluminescent Light-Emitting Transistors Based on CVD-Synthesized Ambipolar ReSe2 Nanosheets. *Adv. Opt. Mater.* **2022**, *10* (8), 9.

(45) O'Brien, M.; McEvoy, N.; Motta, C.; Zheng, J. Y.; Berner, N. C.; Kotakoski, J.; Elibol, K.; Pennycook, T. J.; Meyer, J. C.; Yim, C.; et al. Raman characterization of platinum diselenide thin films. *2D Mater.* **2016**, *3* (2), 7.

(46) Zhao, Y. D.; Qiao, J. S.; Yu, Z. H.; Yu, P.; Xu, K.; Lau, S. P.; Zhou, W.; Liu, Z.; Wang, X. R.; Ji, W.; et al. High-Electron- Mobility and Air-Stable 2D Layered PtSe2 FETs. *Adv. Mater.* **2017**, *29* (5), 10.

(47) Wang, W. J.; Meng, Y.; Wang, W.; Zhang, Z. M.; Xie, P. S.; Lai, Z. X.; Bu, X. M.; Li, Y. Z.; Liu, C. T.; Yang, Z. B.; et al. Highly Efficient Full van der Waals 1D p-Te/2D n-Bi2O2Se Heterodiodes with Nanoscale Ultra-Photosensitive Channels. *Adv. Funct. Mater.* **2022**, *32* (30), 9.

(48) Zhang, J.; Wang, J. H.; Chen, P.; Sun, Y.; Wu, S.; Jia, Z. Y.; Lu, X. B.; Yu, H.; Chen, W.; Zhu, J. Q.; et al. Observation of Strong Interlayer Coupling in MoS2/WS2 Heterostructures. *Adv. Mater.* **2016**, *28* (10), 1950-+.